Nonlinear Dyn (2017) 87:1139–1151
DOI 10.1007/s11071-016-3104-7

ORIGINAL PAPER

Efficiency of non-dimensional analysis for absolute nodal coordinate formulation

Kun-Woo Kim · Jae-Wook Lee · Jin-Seok Jang · Joo-Young Oh · Ji-Heon Kang · Hyung-Ryul Kim · Wan-Suk Yoo

Received: 1 July 2016 / Accepted: 20 September 2016 / Published online: 5 October 2016

Abstract Absolute nodal coordinate formulation was developed in the mid-1990s. The adoption of the continuum mechanics concept has allowed large displacements and large deformations to be expressed in flexible body analysis. However, the analysis time increases due to the increased number of degrees of freedom at nodal points. Therefore, we aimed to reduce the analysis time by converting a dimensional equation of motion (EOM) to a non-dimensional EOM by using non-dimensional variables of time, length, and force. A non-dimensional mass matrix, a non-dimensional longitudinal stiffness matrix, and a non-dimensional conservative force vector are derived and applied to the non-dimensional EOM. To verify the non-dimensional EOM, a cantilever beam with static deflection, for which an exact solution exists, is considered. As the number of elements is increased, the mean value by the non-dimensional EOM converges to the static deflection. Revolute and spherical joints are used to propose two- and three-dimensional numerical solutions based on the non-dimensional EOM of a free-falling pendulum. These solutions are compared with the numerical solutions from using a dimensional EOM in order to verify the non-dimensional EOM. The analysis results for simple pendulum motion using dimensional and non-dimensional EOMs are in good agreement.

Keywords Absolute nodal coordinate formulation · Continuum mechanics · Non-dimensional analysis · Analysis efficiency · Verification of non-dimensional EOM

1 Introduction

Research on absolute nodal coordinate formulation began in 1996 for finite element analysis and the formulation of beams. Absolute nodal coordinate formulation is a non-incremental finite element procedure for flexible body dynamic analysis that is suitable for rigid bodies as well as large displacement and deformation problems [1–8]. In an absolute nodal coordinate formulation, a position vector is expressed as a combina-

K.-W. Kim · J.-W. Lee · J.-S. Jang · J.-Y. Oh · J.-H. Kang
Daegyeong Regional Division, Korea Institute of Industrial Technology, Daegu, South Korea
e-mail: kwkim@kitech.re.kr

J.-W. Lee
e-mail: jaewk@kitech.re.kr

J.-S. Jang
e-mail: jsjang@kitech.re.kr

J.-Y. Oh
e-mail: jyoh@kitech.re.kr

J.-H. Kang
e-mail: kangji1226@kitech.re.kr

H.-R. Kim
Agency for Defense Development, Changwon, South Korea
e-mail: hrkim@add.re.kr

W.-S. Yoo (✉)
School of Mechanical Engineering, Pusan National University, Busan, South Korea
e-mail: wsyoo@pusan.ac.kr

tion of a shape function and nodal coordinate, which can be expressed in various forms by selecting a polynomial depending on the deformation of interest [5,6]. Furthermore, a coordinate transformation matrix based on a rotation angle does not exist because the position vector is directly defined in the global coordinate system. In this way, a mass matrix is defined with a constant. Terms related to the Coriolis force and centrifugal force that occur during the coordinate transformation process are not generated [4,9]. In contrast to a mass matrix expressed with a constant, the stiffness matrix shows a highly nonlinear characteristic. This matrix is based on the concept of a structural mechanics formulation or continuum mechanics [10,11]. Based on this approach, absolute nodal coordinate systems have mainly been used to model strings, strips, drapes, beams, plates, bushings, flexible hoses, tires, and leaf springs where large displacement or large deformation analysis is required [12–18].

When a stiffness matrix is developed with the aforementioned structural mechanics formulation, an Euler–Bernoulli beam [19] can be represented. In this case, the beam element is expressed as a deficient element [4,20]. In other words, because the selection of the position vector gradients related to deformation is limited to the longitudinal direction, the deformation gradient in the lateral direction is not considered. In this case, the deformation information for the lateral direction cannot be confirmed. When a stiffness matrix is developed by using a continuum mechanics approach, a Timoshenko beam is assumed [21], wherein the beam element becomes a fully parameterized element [22]. Thus, the deformation gradients in the lateral and longitudinal directions are considered. Because the deformation information of the cross section is included, the advantage is that the deformation information of the beam can be accurately known. However, for a fully parameterized element with the continuum mechanics approach, shear locking occurs with respect to bending. Because shear locking can hinder the convergence of a numerical solution, various solutions have been proposed [6,11,23]. Among them, the most common solutions are removing a lateral direction term of the shape function polynomial, or increasing the order of the lateral direction term [24,25]. However, removing the lateral direction term has the drawback that the characteristics of large deformation possessed by the absolute nodal coordinate system can be missed because deformation cannot be observed in the cross section. If the order of the lateral direction term is increased, the efficiency of the analysis decreases.

Therefore, the aim of this study was to reduce the analysis time by converting a conventional dimensional equation of motion (EOM) to a non-dimensional EOM for a fully parameterized element. To do this, non-dimensional variables related to the time, length, and force were used. The three-dimensional(3-D) non-dimensional model developed in this study was based on the 3-D model developed by Garcia-Vallejo et al. [22]. For the developed non-dimensional model, the efficiency of the non-dimensional EOM was verified by comparing the CPU time according to the number of elements through examples of a cantilever beam and a free-falling pendulum with revolute and spherical joints.

2 Non-dimensional equation of motion for absolute nodal coordinate formulation

As shown in Fig. 1, an absolute nodal coordinate system is expressed with the global position vector $\vec{\mathbf{r}}$ defined in a global coordinate system and the position vector gradients $\partial\vec{\mathbf{r}}/\partial x$, $\partial\vec{\mathbf{r}}/\partial y$, and $\partial\vec{\mathbf{r}}/\partial z$. As shown in Fig. 1, this comprises a fully parameterized element because the position vector gradients in the y- and z-axis directions (i.e., $\partial\vec{\mathbf{r}}/\partial y$ and $\partial\vec{\mathbf{r}}/\partial z$) are included. Consequently, the physical deformation of the cross section and the deformation in the length direction are considered. As previously noted, because the position vector gradients in the y- and z-axis directions are considered, the analysis time may be increased compared to the gradient-deficient element. As discussed in Sect. 1, the shear locking phenomenon could occur [11,23].

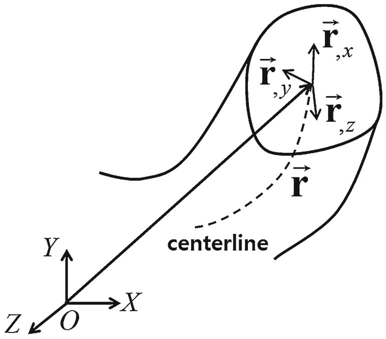

Fig. 1 Absolute nodal coordinate system

The equation for the displacement field suggested by Garcia-Vallejo et al. [22] is expressed as follows:

$$\vec{\mathbf{r}} = \begin{bmatrix} a_0 + a_1 x + a_2 y + a_3 z + a_4 xy + a_5 xz + a_6 x^2 + a_7 x^3 \\ b_0 + b_1 x + b_2 y + b_3 z + b_4 xy + b_5 xz + b_6 x^2 + b_7 x^3 \\ c_0 + c_1 x + c_2 y + c_3 z + c_4 xy + c_5 xz + c_6 x^2 + c_7 x^3 \end{bmatrix} \tag{1}$$

Then, a nodal coordinate can be given as

$$\vec{\mathbf{e}} = \left[\ \vec{\mathbf{r}}|_{x=0}^{T}\ \ \frac{\partial\,\vec{\mathbf{r}}|_{x=0}^{T}}{\partial x}\ \ \frac{\partial\,\vec{\mathbf{r}}|_{x=0}^{T}}{\partial y}\ \ \frac{\partial\,\vec{\mathbf{r}}|_{x=0}^{T}}{\partial z}\ \ \vec{\mathbf{r}}|_{x=l_e}^{T}\ \ \frac{\partial\,\vec{\mathbf{r}}|_{x=l_e}^{T}}{\partial x}\ \ \frac{\partial\,\vec{\mathbf{r}}|_{x=l_e}^{T}}{\partial y}\ \ \frac{\partial\,\vec{\mathbf{r}}|_{x=l_e}^{T}}{\partial z}\ \right]^{\mathrm{T}} \tag{2}$$

where x is an arbitrary point following a neutral axis of the element for the state before deformation and l_e is the length of the element.

The nodal coordinate ($\vec{\mathbf{e}}$) and shape function ($\mathbf{S}$) for the element before deformation comprise the global position vector ($\vec{\mathbf{r}}$), as shown in Eq. (3) from Eq. (1), by boundary conditions at $x = 0$ and $x = l_e$.

$$\vec{\mathbf{r}} = \left[r_1\ r_2\ r_3 \right]^{\mathrm{T}} = \mathbf{S}\vec{\mathbf{e}} \tag{3}$$

Next, the shape function in Eq. (3) is given as follows:

$$\mathbf{S} = \left[S_1\mathbf{I}\quad S_2\mathbf{I}\quad S_3\mathbf{I}\quad S_4\mathbf{I}\quad S_5\mathbf{I}\quad S_6\mathbf{I}\quad S_7\mathbf{I}\quad S_8\mathbf{I} \right] \tag{4}$$

where $\mathbf{I}$ is a 3×3 identity matrix in 3D, $S_i = S_i(\xi, \eta, \zeta)$ $(i = 1 \sim 8)$ is defined in Eq. (5), and ξ, η, and ζ are non-dimensionalized values that refer to $\xi = x/l_e$, $\eta = y/l_e$, and $\varsigma = z/l_e$. Thus,

$$\begin{aligned} &S_1 = 1 - 3\xi^2 + 2\xi^3, && S_2 = l_e\left(\xi - 2\xi^2 + 3\xi^3\right), \\ &S_3 = l_e\left(\eta - \xi\eta\right), && S_4 = l_e\left(\varsigma - \xi\varsigma\right), \\ &S_5 = 3\xi^2 - 2\xi^3, && S_6 = l_e\left(\xi^3 - \xi^2\right), \\ &S_7 = l_e\left(\xi\eta\right) && S_8 = l_e\left(\xi\varsigma\right) \end{aligned} \tag{5}$$

The global position vector in Eq. (3) is $\vec{\mathbf{r}} = \vec{\mathbf{r}}(\xi, \eta, \varsigma, t)$, i.e., it is a variable for space and time functions. The shape function $\mathbf{S} = \mathbf{S}(\xi, \eta, \varsigma)$ is a variable for the space function. The nodal coordinate $\vec{\mathbf{e}} = \vec{\mathbf{e}}(t)$ is a variable for the time function. Based on the relationships of the shape function with respect to the space and time functions of the nodal coordinate, the mass matrix, stiffness matrix, and the conservative force vector can be determined as follows:

$$\mathbf{M}\ddot{\vec{\mathbf{e}}} + \mathbf{K}(\vec{\mathbf{e}})\vec{\mathbf{e}} = \vec{\mathbf{F}}_C \tag{6}$$

where $\mathbf{M}$ is the mass matrix, $\mathbf{K}$ is the stiffness matrix, and $\vec{\mathbf{F}}_C$ is the conservative force vector corresponding to gravity.

During the non-dimensionalization process of the EOM, T_{ND} can be used as a non-dimensional variable of time, as follows [26]:

$$t = T_{\mathrm{ND}} t^* \quad \left(T_{\mathrm{ND}} = L_{\mathrm{ND}} \sqrt{\frac{\rho A}{F_{\mathrm{ND}}}} \right) \tag{7}$$

where t is the time, ρ is the density, A is the cross-sectional area, L_{ND} is a non-dimensional length for the maximum length of the beam, and F_{ND} is an arbitrary force acting on the beam and represents a non-dimensional force unit. Note that * means a non-dimensionalized variable. There is a difference between the physical time versus the actual analysis time according to the non-dimensional variable T_{ND} in Eq. (7). When T_{ND} is greater than 1, the process is efficient because the physical time is greater than the analysis time. As shown in Eq. (7), for T_{ND}, the analysis efficiency of the non-dimensional EOM increases with L_{ND}.

The non-dimensional variable for the length can be expressed for a non-dimensional EOM as follows:

$$x = L_{\mathrm{ND}} x^*, \quad l_e = L_{\mathrm{ND}} l_{\mathrm{e}}^*, \quad \hat{\vec{\mathbf{e}}} = L_{\mathrm{ND}} \hat{\vec{\mathbf{e}}}^* \tag{8}$$

where the caret symbol (^) above the characters indicates a newly defined shape function and nodal coordinate that differs from those in Eq. (3). In Eq. (3), the dimensions of the shape function and nodal coordinate are mixed. In other words, because the dimensions and non-dimension are mixed with each other, a somewhat complex process is required to non-dimensionalize the EOM in Eq. (6). Therefore, it is necessary to unify each dimension of the shape function and nodal coordinate with respect to non-dimensionalization. In this study, the shape function was determined to be non-dimensional, and the dimension of the nodal coordinate was determined to be the length. Therefore, the position vector of Eq. (3) can be defined as

$$\vec{\mathbf{r}} = \hat{\mathbf{S}}\hat{\vec{\mathbf{e}}} \tag{9}$$

Because the coordinates corresponding to the nodal slopes of Eq. (2) are multiplied by the length of element l_e, the nodal slopes can be represented by the length dimension rather than being non-dimensional, as follows:

$$\hat{\vec{\mathbf{e}}} = \left[\vec{\mathbf{r}}|_{x=0}^{T} \; l_e \frac{\partial\, \vec{\mathbf{r}}|_{x=0}^{T}}{\partial x} \; l_e \frac{\partial\, \vec{\mathbf{r}}|_{x=0}^{T}}{\partial y} \; l_e \frac{\partial\, \vec{\mathbf{r}}|_{x=0}^{T}}{\partial z} \; \vec{\mathbf{r}}|_{x=l_e}^{T} \; l_e \frac{\partial\, \vec{\mathbf{r}}|_{x=l_e}^{T}}{\partial x} \; l_e \frac{\partial\, \vec{\mathbf{r}}|_{x=l_e}^{T}}{\partial y} \; l_e \frac{\partial\, \vec{\mathbf{r}}|_{x=l_e}^{T}}{\partial z} \right]^{\mathrm{T}} \tag{10}$$

The shape function is defined as non-dimensional, as shown in Eq. (11). The shape function newly defined by Eq. (11) can be expressed with Eq. (11):

$$\hat{\mathbf{S}} = \left[S_1\mathbf{I} \quad \hat{S}_2\mathbf{I} \quad \hat{S}_3\mathbf{I} \quad \hat{S}_4\mathbf{I} \quad S_5\mathbf{I} \quad \hat{S}_6\mathbf{I} \quad \hat{S}_7\mathbf{I} \quad \hat{S}_8\mathbf{I} \right] \tag{11}$$

where the components of the newly defined shape function are defined as

$$\begin{aligned} S_1 &= 1 - 3\xi^2 + 2\xi^3, & \hat{S}_2 &= \xi - 2\xi^2 + 3\xi^3, \\ \hat{S}_3 &= \eta - \xi\eta, & \hat{S}_4 &= \varsigma - \xi\varsigma, \\ S_5 &= 3\xi^2 - 2\xi^3, & \hat{S}_6 &= l_e\left(\xi^3 - \xi^2\right), \\ \hat{S}_7 &= \xi\eta & \hat{S}_8 &= \xi\varsigma \end{aligned} \tag{12}$$

By using Eq. (9) and the non-dimensional variable L_{ND}, the non-dimensional global position vector can be defined as

$$\vec{\mathbf{r}} = L_{\mathrm{ND}}\vec{\mathbf{r}}^{*} = \hat{\mathbf{S}}\hat{\vec{\mathbf{e}}} = L_{\mathrm{ND}}\hat{\mathbf{S}}\hat{\vec{\mathbf{e}}}^{*} \quad \rightarrow \quad \vec{\mathbf{r}}^{*} = \hat{\mathbf{S}}\hat{\vec{\mathbf{e}}}^{*} \tag{13}$$

The non-dimensional mass matrix, non-dimensional stiffness matrix, and non-dimensional external conservative force can be determined as shown in Eq. (14) by using the newly defined non-dimensional position vector of Eq. (13):

$$\mathbf{M}^{*}\left(\frac{\mathrm{d}^2\hat{\vec{\mathbf{e}}}^{*}}{\mathrm{d}t^{*2}}\right) + \mathbf{K}^{*}(\hat{\vec{\mathbf{e}}}^{*})\hat{\vec{\mathbf{e}}}^{*} = \vec{\mathbf{F}}_{C}^{*} \tag{14}$$

where the non-dimensional nodal coordinate $\hat{\vec{\mathbf{e}}}^{*}$ is the value of the nodal coordinate in Eq. (10) when non-dimensionalized by the relationship in Eq. (13). This yields

$$\hat{\vec{\mathbf{e}}}^{*} = \left[\vec{\mathbf{r}}^{*}|_{x^{*}=0}^{T} \; l_{\mathrm{e}}^{*} \frac{\partial\, \vec{\mathbf{r}}^{*}|_{x^{*}=0}^{T}}{\partial x^{*}} \; l_{\mathrm{e}}^{*} \frac{\partial\, \vec{\mathbf{r}}^{*}|_{x^{*}=0}^{T}}{\partial y^{*}} \; l_{\mathrm{e}}^{*} \frac{\partial\, \vec{\mathbf{r}}^{*}|_{x^{*}=0}^{T}}{\partial z^{*}} \; \vec{\mathbf{r}}^{*}|_{x^{*}=l_{\mathrm{e}}^{*}}^{T} \; l_{\mathrm{e}}^{*} \frac{\partial\, \vec{\mathbf{r}}^{*}|_{x^{*}=l_{\mathrm{e}}^{*}}^{T}}{\partial x^{*}} \; l_{\mathrm{e}}^{*} \frac{\partial\, \vec{\mathbf{r}}^{*}|_{x^{*}=l_{\mathrm{e}}^{*}}^{T}}{\partial y^{*}} \; l_{\mathrm{e}}^{*} \frac{\partial\, \vec{\mathbf{r}}^{*}|_{x^{*}=l_{\mathrm{e}}^{*}}^{T}}{\partial z^{*}} \right]^{\mathrm{T}} \tag{15}$$

A non-dimensional EOM to express a flexible body consists of a mechanical or multi-body system with inter-constraints. The differential algebraic equation (DAE) includes a Lagrange multiplier along with a constraint equation, which is given by [27]

$$\vec{\boldsymbol{\Psi}}\left(\frac{\mathrm{d}^2\hat{\vec{\mathbf{e}}}^{*}}{\mathrm{d}t^{*2}}, \vec{\boldsymbol{\lambda}}\right) = \begin{bmatrix} \mathbf{M}^{*}\left(\frac{\mathrm{d}^2\hat{\vec{\mathbf{e}}}^{*}}{\mathrm{d}t^{*2}}\right) + \boldsymbol{\Phi}_{\hat{\vec{\mathbf{e}}}^{*}}^{T}\vec{\boldsymbol{\lambda}} + \mathbf{K}^{*}(\hat{\vec{\mathbf{e}}}^{*})\hat{\vec{\mathbf{e}}}^{*} - \vec{\mathbf{F}}_{C}^{*} \\ \vec{\boldsymbol{\Phi}}\left(\hat{\vec{\mathbf{e}}}^{*}\right) \end{bmatrix} = \vec{\mathbf{0}} \tag{16}$$

where $\vec{\boldsymbol{\Phi}}$ is the constraint equation, $\boldsymbol{\Phi}_{\hat{\vec{\mathbf{e}}}^{*}}^{T}$ is the Jacobian matrix of the constraint equation, and $\vec{\boldsymbol{\lambda}}$ is the Lagrange multiplier. Equation (16) is a DAE of index 3 [28]. In this study, the numerical solution to Eq. (16) was obtained at each time step through Newmark implicit integration [29,30]. The numerical solution for Eq. (16) is included in Appendix 1.

The processes of determining the non-dimensional mass matrix ($\mathbf{M}^{*}$), non-dimensional stiffness matrix ($\mathbf{K}^{*}$), and non-dimensional conservative force corresponding to gravity ($\vec{\mathbf{F}}_{C}^{*}$) are given in Sects. 2.1, 2.2, and 2.3, respectively. As previously noted, the non-dimensional EOM developed in this study was based on the dimensional EOM developed by Garcia-Vallejo et al. [22].

2.1 Non-dimensional mass matrix

The kinetic energy is necessary to derive the non-dimensional mass matrix which can be determined as shown in Eq. (17) by using the variables L_{ND}, T_{ND}, and F_{ND}, which represent the non-dimensional length, time, and force, respectively:

$$\begin{aligned} T &= \frac{1}{2}\int_A \int_0^{l_e} \rho \left(\frac{\partial \vec{\mathbf{r}}}{\partial t}\right)^{\mathrm{T}} \left(\frac{\partial \vec{\mathbf{r}}}{\partial t}\right) \mathrm{d}x\mathrm{d}A \\ &= \frac{1}{2}\frac{L_{\mathrm{ND}}^5}{T_{\mathrm{ND}}^2}\int_{A^*} \int_0^{l_{\mathrm{e}}^*} \rho \left(\frac{\partial \vec{\mathbf{r}}^*}{\partial t^*}\right)^{\mathrm{T}} \left(\frac{\partial \vec{\mathbf{r}}^*}{\partial t^*}\right) \mathrm{d}x^*\mathrm{d}A^* \\ &= \frac{1}{2}\frac{L_{\mathrm{ND}}^3}{A}F_{\mathrm{ND}}\int_{A^*} \int_0^{l_{\mathrm{e}}^*} \left(\frac{\partial \vec{\mathbf{r}}^*}{\partial t^*}\right)^{\mathrm{T}} \left(\frac{\partial \vec{\mathbf{r}}^*}{\partial t^*}\right) \mathrm{d}x^*\mathrm{d}A^* \end{aligned} \tag{17}$$

Based on Eq. (17), the non-dimensional EOM can be determined as

$$\begin{aligned} T^* &= \frac{1}{2}\int_{A^*} \int_0^{l_{\mathrm{e}}^*} \left(\frac{\partial \vec{\mathbf{r}}^*}{\partial t^*}\right)^{\mathrm{T}} \left(\frac{\partial \vec{\mathbf{r}}^*}{\partial t^*}\right) \mathrm{d}x^*\mathrm{d}A^* \\ &= \frac{1}{2}\left(\frac{\partial \hat{\vec{\mathbf{e}}}^*}{\partial t^*}\right)\int_{A^*} \int_0^{l_{\mathrm{e}}^*} \left(\hat{\mathbf{S}}\right)^{\mathrm{T}} \left(\hat{\mathbf{S}}\right) \mathrm{d}x^*\mathrm{d}A^*\left(\frac{\partial \hat{\vec{\mathbf{e}}}^*}{\partial t^*}\right) \end{aligned} \tag{18}$$

Therefore, the non-dimensional mass matrix can be determined as

$$\begin{aligned} \mathbf{M}^* &= \textstyle\int_{A^*} \int_0^{l_{\mathrm{e}}^*} \left(\hat{\mathbf{S}}\right)^{\mathrm{T}} \left(\hat{\mathbf{S}}\right) \mathrm{d}x^*\mathrm{d}A^* \\ &= l_{\mathrm{e}}^* \textstyle\int_{A^*} \int_0^{1} \left(\hat{\mathbf{S}}\right)^{\mathrm{T}} \left(\hat{\mathbf{S}}\right) \mathrm{d}\xi\mathrm{d}A^* \end{aligned} \tag{19}$$

2.2 Non-dimensional stiffness matrix

In this study, the continuum mechanics approach was used to determine the non-dimensional stiffness matrix from the non-dimensional strain energy [8,10,22]. First, the deformation gradient expressed by the nonlinear Green–Lagrange strain–displacement relationship is given in Eq. (20). The deformation gradient is itself non-dimensional because it is defined from the non-dimensional position vector in this study. Thus, the previously applied symbol of "$*$" representing non-dimensionality is used.

$$\mathbf{J}^* = \frac{\partial \vec{\mathbf{r}}^*}{\partial \vec{\mathbf{r}}_0^*} = \frac{\partial \vec{\mathbf{r}}^*}{\partial \vec{\mathbf{x}}^*}\frac{\partial \vec{\mathbf{x}}^*}{\partial \vec{\mathbf{r}}_0^*} = \frac{\partial \vec{\mathbf{r}}^*}{\partial \vec{\mathbf{x}}^*}\mathbf{J}_0^{*(-1)} = \frac{\partial \vec{\mathbf{r}}^*}{\partial \vec{\mathbf{x}}^*} \tag{20}$$

In Eq. (20), $\vec{\mathbf{r}}_0^*$ is the non-dimensional position vector of the element before deformation, and $\vec{\mathbf{x}}^*$ is a component defined at the local coordinate of the element before deformation where $\vec{\mathbf{x}}^* = \left[\, x^*\ y^*\ z^* \,\right]^{\mathrm{T}}$. In addition, $\mathbf{J}_0^* = \partial \vec{\mathbf{r}}_0^* / \partial \vec{\mathbf{x}}^*$: as a deformation gradient for the coordinate before deformation, it is expressed with an identity matrix. Therefore, Eq. (20) can also be expressed as

$$\mathbf{J}^* = \left[\, \hat{\mathbf{S}}_{,1}\,\hat{\vec{\mathbf{e}}}^*\ \hat{\mathbf{S}}_{,2}\,\hat{\vec{\mathbf{e}}}^*\ \hat{\mathbf{S}}_{,3}\,\hat{\vec{\mathbf{e}}}^* \,\right] \tag{21}$$

where $\hat{\mathbf{S}}_{,\alpha}$ is $\partial \hat{\mathbf{S}} / \partial \alpha$, and $\alpha = 1, 2, 3$ refers to $\alpha = x^*, y^*, z^*$.

Next, if the deformation gradient is used, the strain tensor can be determined as shown in Eq. (22). Although the strain tensor is also non-dimensional, the $*$ symbol is still used to signify non-dimensionality.

$$\vec{\boldsymbol{\varepsilon}}^* = \frac{1}{2}\left(\mathbf{J}^{*T}\mathbf{J}^* - \mathbf{I}\right) = \left[\, \varepsilon_{11}^*\ \varepsilon_{22}^*\ \varepsilon_{33}^*\ \varepsilon_{12}^*\ \varepsilon_{13}^*\ \varepsilon_{23}^* \,\right]^{\mathrm{T}} \tag{22}$$

Therefore, if Eq. (22) is assumed to be a symmetric strain tensor, the six different components are given by

$$\begin{aligned} &\varepsilon_{11}^* = \tfrac{1}{2}\left(\hat{\vec{\mathbf{e}}}^{*T}\hat{\mathbf{S}}_{,x^*}^{T}\,\hat{\mathbf{S}}_{,x^*}\,\hat{\vec{\mathbf{e}}}^* - 1\right), \quad &\varepsilon_{12}^* = \tfrac{1}{2}\left(\hat{\vec{\mathbf{e}}}^{*T}\hat{\mathbf{S}}_{,x^*}^{T}\,\hat{\mathbf{S}}_{,y^*}\,\hat{\vec{\mathbf{e}}}^*\right), \\ &\varepsilon_{22}^* = \tfrac{1}{2}\left(\hat{\vec{\mathbf{e}}}^{*T}\hat{\mathbf{S}}_{,y^*}^{T}\,\hat{\mathbf{S}}_{,y^*}\,\hat{\vec{\mathbf{e}}}^* - 1\right), \quad &\varepsilon_{13}^* = \tfrac{1}{2}\left(\hat{\vec{\mathbf{e}}}^{*T}\hat{\mathbf{S}}_{,x^*}^{T}\,\hat{\mathbf{S}}_{,z^*}\,\hat{\vec{\mathbf{e}}}^*\right), \\ &\varepsilon_{33}^* = \tfrac{1}{2}\left(\hat{\vec{\mathbf{e}}}^{*T}\hat{\mathbf{S}}_{,z^*}^{T}\,\hat{\mathbf{S}}_{,z^*}\,\hat{\vec{\mathbf{e}}}^* - 1\right), \quad &\varepsilon_{23}^* = \tfrac{1}{2}\left(\hat{\vec{\mathbf{e}}}^{*T}\hat{\mathbf{S}}_{,y^*}^{T}\,\hat{\mathbf{S}}_{,z^*}\,\hat{\vec{\mathbf{e}}}^*\right) \end{aligned} \tag{23}$$

If a flexible body is assumed to be an isotropic homogeneous material, the relationship between stresses and strains can be written explicitly as follows [10]:

$$\begin{aligned} \sigma_{ij} &= \lambda\left(\varepsilon_{11} + \varepsilon_{22} + \varepsilon_{33}\right) + 2G\varepsilon_{ii}, \quad i = 1, 2, 3 \\ \sigma_{ij} &= 2G\varepsilon_{ij}, \quad i \neq j \end{aligned} \tag{24}$$

where λ is Lame's constant and G is the shear modulus. Then, the stress vector can be expressed as

$$\vec{\boldsymbol{\sigma}} = \mathbf{E}\vec{\boldsymbol{\varepsilon}} = \left[\, \sigma_{11}\ \sigma_{22}\ \sigma_{33}\ \sigma_{12}\ \sigma_{13}\ \sigma_{23} \,\right]^{\mathrm{T}} \tag{25}$$

where $\mathbf{E}$ is the matrix of elastic coefficients.

Using Eqs. (22) and (25), the strain energy can be expressed as [31]

$$\begin{aligned} U &= \frac{1}{2}\int_A \int_0^{l_e} \boldsymbol{\sigma}^{\mathrm{T}}\boldsymbol{\varepsilon}\ \mathrm{d}x\mathrm{d}A \\ &= \frac{1}{2}\int_A \int_0^{l_e} \boldsymbol{\varepsilon}^{\mathrm{T}}\mathbf{E}\boldsymbol{\varepsilon}\ \mathrm{d}x\mathrm{d}A \\ &= \frac{1}{2}F_{\mathrm{ND}}L_{\mathrm{ND}}\int_{A^*} \int_0^{l_{\mathrm{e}}^*} \boldsymbol{\varepsilon}^{*T}\mathbf{E}^*\boldsymbol{\varepsilon}^*\ \mathrm{d}x^*\mathrm{d}A^* \end{aligned} \tag{26}$$

where $\mathbf{E}^*$ is the non-dimensional matrix of elastic coefficients and is equal to $\left(L_{\mathrm{ND}}^2 / F_{\mathrm{ND}}\right)\mathbf{E}$.

Therefore, the non-dimensional strain energy can be expressed as shown in Eq. (27):

$$U^* = \frac{1}{2}\int_{A^*}\int_0^{l_e^*} \boldsymbol{\varepsilon}^{*T}\mathbf{E}^*\boldsymbol{\varepsilon}^*\,\mathrm{d}x^*\mathrm{d}A^*$$
$$= \frac{1}{2}\int_{A^*}\int_0^{l_e^*}\begin{bmatrix} \frac{(\lambda+2G)}{(F_{\mathrm{ND}}/L_{\mathrm{ND}}^2)}\left(\varepsilon_{11}^{*2}+\varepsilon_{22}^{*2}+\varepsilon_{33}^{*2}\right) \\ +\frac{\lambda}{(F_{\mathrm{ND}}/L_{\mathrm{ND}}^2)}\left(\varepsilon_{11}^*\varepsilon_{22}^*+\varepsilon_{11}^*\varepsilon_{33}^*+\varepsilon_{22}^*\varepsilon_{33}^*\right) \\ +\frac{2G}{(F_{\mathrm{ND}}/L_{\mathrm{ND}}^2)}\left(\varepsilon_{12}^{*2}+\varepsilon_{13}^{*2}+\varepsilon_{23}^{*2}\right)\end{bmatrix}$$
$$\mathrm{d}x^*\mathrm{d}A^* \qquad (27)$$

and where ν is Poisson's ratio, and E is Young's modulus. Therefore, from Eq. (27), the elastic force can be determined as follows:

$$\mathbf{F}_e^* = -\frac{\partial U^*}{\partial\hat{\vec{\mathbf{e}}}^*}$$
$$= -\frac{1}{2}\int_{A^*}\int_0^{l_e^*}$$
$$\times\begin{bmatrix} \frac{(\lambda+2G)}{(F_{\mathrm{ND}}/L_{\mathrm{ND}}^2)}\left(2\frac{\partial\varepsilon_{11}^*}{\partial\hat{\vec{\mathbf{e}}}^*}\varepsilon_{11}^*+2\frac{\partial\varepsilon_{22}^*}{\partial\hat{\vec{\mathbf{e}}}^*}\varepsilon_{22}^*+2\frac{\partial\varepsilon_{33}^*}{\partial\hat{\vec{\mathbf{e}}}^*}\varepsilon_{33}^*\right) \\ +\frac{\lambda}{(F_{\mathrm{ND}}/L_{\mathrm{ND}}^2)}\begin{pmatrix} \frac{\partial\varepsilon_{11}^*}{\partial\hat{\vec{\mathbf{e}}}^*}\varepsilon_{22}^*+\frac{\partial\varepsilon_{22}^*}{\partial\hat{\vec{\mathbf{e}}}^*}\varepsilon_{11}^*+\frac{\partial\varepsilon_{11}^*}{\partial\hat{\vec{\mathbf{e}}}^*}\varepsilon_{33}^* \\ +\frac{\partial\varepsilon_{33}^*}{\partial\hat{\vec{\mathbf{e}}}^*}\varepsilon_{11}^*+\frac{\partial\varepsilon_{22}^*}{\partial\hat{\vec{\mathbf{e}}}^*}\varepsilon_{33}^*+\frac{\partial\varepsilon_{33}^*}{\partial\hat{\vec{\mathbf{e}}}^*}\varepsilon_{22}^*\end{pmatrix} \\ +\frac{2G}{(F_{\mathrm{ND}}/L_{\mathrm{ND}}^2)}\left(2\frac{\partial\varepsilon_{12}^*}{\partial\hat{\vec{\mathbf{e}}}^*}\varepsilon_{12}^*+2\frac{\partial\varepsilon_{13}^*}{\partial\hat{\vec{\mathbf{e}}}^*}\varepsilon_{13}^*+2\frac{\partial\varepsilon_{23}^*}{\partial\hat{\vec{\mathbf{e}}}^*}\varepsilon_{23}^*\right)\end{bmatrix}$$
$$\times\mathrm{d}x^*\mathrm{d}A^* \qquad (28)$$

From Eq. (28), the derivative term for the non-dimensional nodal coordinate of the strain tensor component is given by

$$\frac{\partial\varepsilon_{ij}^*}{\partial\hat{\vec{\mathbf{e}}}^*} = \frac{1}{2}\left(\hat{\mathbf{S}}_{,i}^T\hat{\mathbf{S}}_{,j}+\hat{\mathbf{S}}_{,j}^T\hat{\mathbf{S}}_{,i}\right)\hat{\vec{\mathbf{e}}}^* \quad (i, j = 1, 2, 3 \quad j \geq i) \qquad (29)$$

Substituting Eq. (29) into Eq. (28) and rearranging yield

$$\mathbf{F}_e^* = -\mathbf{K}(\hat{\vec{\mathbf{e}}}^*)\hat{\vec{\mathbf{e}}}^* \qquad (30)$$

Therefore, the non-dimensional stiffness matrix is given by

$$\mathbf{K}^*(\hat{\vec{\mathbf{e}}}^*) = \sum_{\alpha=1}^{3}\frac{(\lambda+2G)}{2(F_{\mathrm{ND}}/L_{\mathrm{ND}}^2)}$$
$$\times\int_{A^*}\int_0^{l_e^*}\left(\hat{\mathbf{S}}_{,\alpha}^T\hat{\mathbf{S}}_{,\alpha}\hat{\vec{\mathbf{e}}}^*\hat{\vec{\mathbf{e}}}^{*T}\hat{\mathbf{S}}_{,\alpha}^T\hat{\mathbf{S}}_{,\alpha}-\hat{\mathbf{S}}_{,\alpha}^T\hat{\mathbf{S}}_{,\alpha}\right)$$
$$\times\,\mathrm{d}x^*\mathrm{d}A^*$$
$$+\sum_{\alpha=1}^{3}\sum_{\substack{\beta=1\\ \beta\neq\alpha}}^{3}\frac{\lambda}{2(F_{\mathrm{ND}}/L_{\mathrm{ND}}^2)}$$
$$\times\int_{A^*}\int_0^{l_e^*}\left(\hat{\mathbf{S}}_{,\alpha}^T\hat{\mathbf{S}}_{,\alpha}\hat{\vec{\mathbf{e}}}^*\hat{\vec{\mathbf{e}}}^{*T}\hat{\mathbf{S}}_{,\beta}^T\hat{\mathbf{S}}_{,\beta}-\hat{\mathbf{S}}_{,\alpha}^T\hat{\mathbf{S}}_{,\alpha}\right)$$
$$\times\mathrm{d}x^*\mathrm{d}A^*$$
$$+\sum_{\alpha=1}^{3}\sum_{\substack{\beta=1\\ \beta\neq\alpha}}^{3}\frac{G}{(F_{\mathrm{ND}}/L_{\mathrm{ND}}^2)}$$
$$\times\int_{A^*}\int_0^{l_e^*}\left(\hat{\mathbf{S}}_{,\alpha}^T\hat{\mathbf{S}}_{,\beta}\hat{\vec{\mathbf{e}}}^*\hat{\vec{\mathbf{e}}}^{*T}\hat{\mathbf{S}}_{,\alpha}^T\hat{\mathbf{S}}_{,\beta}\right)\mathrm{d}x^*\mathrm{d}A^* \qquad (31)$$

2.3 Non-dimensional conservative force vector

For the conservative force corresponding to gravity, a distributed load should be considered rather than a concentrated load. Using the non-dimensional variables F_{ND} and L_{ND} for the force and length, respectively, we obtain

$$\vec{\mathbf{F}}_C^T = \int_A\int_0^{l_e}\rho\vec{\mathbf{G}}^{\mathrm{T}}\hat{\mathbf{S}}\,\mathrm{d}x\mathrm{d}A$$
$$= F_{\mathrm{ND}}\int_{A^*}\int_0^{l_e^*}\frac{\rho\vec{\mathbf{G}}^{\mathrm{T}}\hat{\mathbf{S}}}{(F_{\mathrm{ND}}/L_{\mathrm{ND}}^3)}\,\mathrm{d}x^*\mathrm{d}A^* \qquad (32)$$

where $\vec{\mathbf{G}}$ is a vector containing the acceleration of gravity.

Therefore, the non-dimensional conservative force can be expressed as

$$\vec{\mathbf{F}}_C^{*T} = \int_{A^*}\int_0^{l_e^*}\frac{\rho\vec{\mathbf{G}}^{\mathrm{T}}\hat{\mathbf{S}}}{(F_{\mathrm{ND}}/L_{\mathrm{ND}}^3)}\,\mathrm{d}x^*\mathrm{d}A^* \qquad (33)$$

3 Verification of non-dimensional equation of motion

As discussed in Sect. 2, a non-dimensional EOM was determined by using the non-dimensional variables L_{ND}, T_{ND}, and F_{ND} representing the length, time, and force, respectively. In this section, the non-dimensional EOM is compared with the dimensional EOM based on the examples of a cantilever beam and free-falling pendulum with revolute and spherical joints for verification. Table 1 gives the specifications of the personal computer used in this study. MATLAB® [32] was used to verify the non-dimensional EOM because some successful applications have been based on this software [33–37].

Table 1 Computer specifications for analysis

CPU	Intel® Core^{TM} i7-4930 K @ 3.40 GHz
Memory capacity	32 GB
Commercial software	MATLAB R2012a - 64 bit

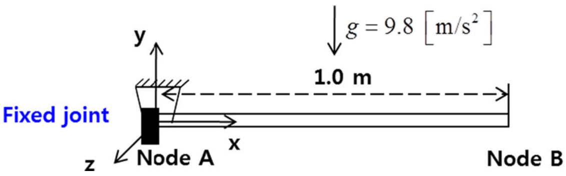

Fig. 2 Cantilever beam

Table 2 Properties and data of free-falling pendulum

Density (kg/m^3)	Modulus of elasticity (N/m^2)	Length (m)	Diameter (m)
8030	193E+09	1.00	0.20

Table 3 Non-dimensional parameter T_{ND} for various numbers of elements

	Number of elements					
	1	2	5	10	15	20
T_{ND}	0.32 s	0.45 s	0.71 s	1.01 s	1.24 s	1.43 s

3.1 Cantilever beam

To verify the non-dimensional EOM, a cantilever beam with an exact solution for static deflection is considered, as shown in Fig. 2. Table 2 gives the specifications of the cantilever beam and the physical properties of 304 stainless steel.

As given in Table 3, the non-dimensional time variable T_{ND} in Eq. (7) for the non-dimensional EOM is determined by the number of elements.

When the data in Table 3 were interpreted by using Eq. (7), the physical time was less than the analysis time when $T_{ND} < 1$, and the physical time was more than the analysis time when $T_{ND} > 1$. Table 4 presents the calculation time for a physical time of 2 s for the cantilever beam when using the dimensional and non-dimensional EOMs. Figure 3 shows a graph the numerical values from Table 4. The efficiency in terms of the calculation time was confirmed to increase when the non-dimensional variable T_{ND} and the number of elements increase. In particular, when there were 20 elements, the calculation time efficiency was increased approximately twofold. When there were 10 elements, despite the non-dimensional variable T_{ND} being close to unity, using the non-dimensional EOM was more advantageous in terms of the calculation time because the convergence of solutions increased during the process of finding a solution at each step.

Table 4 Analysis time of dimensional and non-dimensional equations of motion for various numbers of elements representing the cantilever beam

	Number of elements					
	1 (s)	2 (s)	5 (s)	10 (s)	15 (s)	20 (s)
DIM	6.27	16.28	41.90	109.64	166.69	231.52
Non-DIM	28.45	38.65	54.67	93.63	114.47	131.04

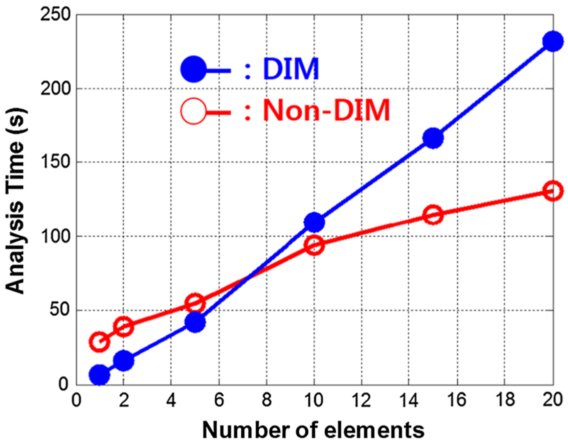

Fig. 3 Comparison of analysis times with dimensional and non-dimensional equations of motion

For the case of a distributed load acting on the cantilever beam, Eq. (34) shows the calculated static deflection at the end node of the cantilever beam described in Table 2:

$$\delta = \frac{qL^4}{8EI} \cong -2.040\ mm \tag{34}$$

where δ is the static deflection at the end node of the cantilever beam, q is the distributed load, L is the cantilever beam's length, E is the Young's modulus, and I is the area moment of inertia.

Table 5 Mean value of deflection for various numbers of elements with dimensional and non-dimensional equations of motion

	Number of elements					
	1 (mm)	2 (mm)	5 (mm)	10 (mm)	15 (mm)	20 (mm)
DIM	−1.357	−1.870	−2.014	−2.032	−2.036	−2.037
Non-DIM	−1.356	−1.872	−2.015	−2.032	−2.036	−2.037

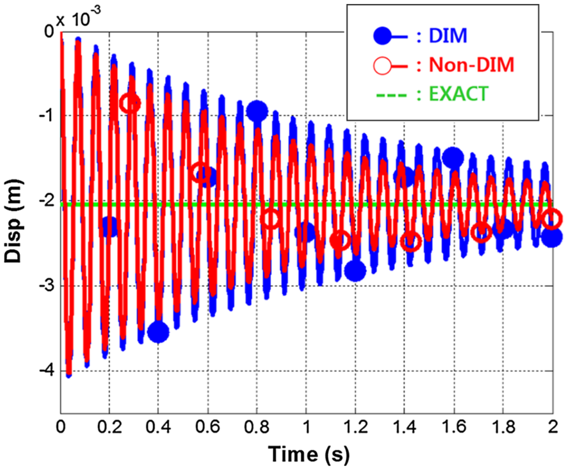

Fig. 4 Exact solution and mean value of deflection for 20 elements with dimensional and non-dimensional equations of motion

Table 5 presents the mean value of deflection at the end node of the cantilever beam when the physical time was set according to the number of elements at 2 s. As the number of elements increased, the mean value converges to the static deflection. With 20 elements, Fig. 4 shows that the mean value is nearly the same as the static deflection. The damping in Fig. 4 is a numerical value, not structural damping. In this study, $\gamma = 0.70$ and $\beta = 0.36$ were selected as introduced in ADAMS [38].

As listed in Table 5 and Fig. 5, when the analysis had an insufficient number of elements, shear locking was confirmed to occur. When the number of elements was insufficient, physically nonexistent shear strain greatly increased numerically, and the deflection of the cantilever beam was reduced. In other words, the normal strain, which must occur in the direction of deflection, decreased. Therefore, a solution close to an exact solution can be obtained when the system is divided into a sufficient number of elements.

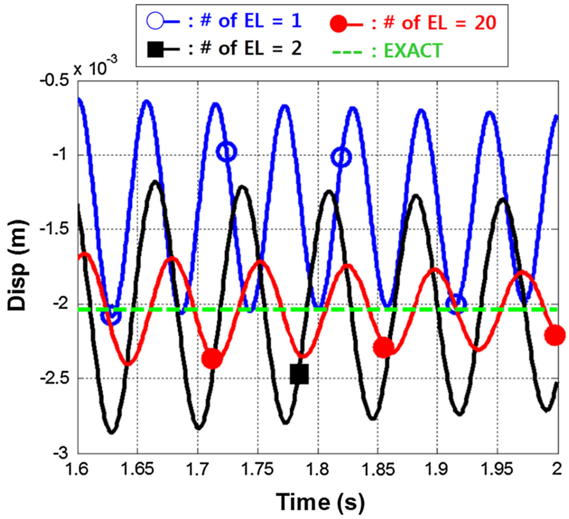

Fig. 5 Exact solution and shear locking phenomenon by number of elements

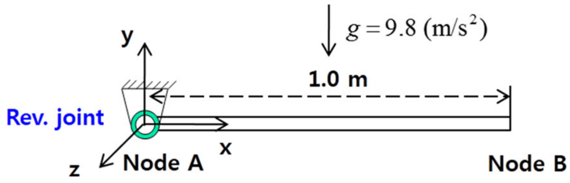

Fig. 6 Free-falling pendulum with revolute joint

Table 6 Data for analysis of simple pendulum attached to revolute joint with dimensional and non-dimensional equations of motion

	DIM	Non-DIM
Number of elements	1	1 ($T_{\mathrm{ND}} = 0.32$ s)
Step size	0.00100 s	0.00032 s
Number of iteration	2001	6263
Analysis time	37.62 s	27.96 s

3.2 Free-falling pendulum with revolute joint

The free-falling pendulum with a revolute joint example shown in Fig. 6 was used to compare the calculation times of dimensional and non-dimensional EOMs and verify the accuracy of the numerical solution. The specifications and physical properties for a simple pendulum motion are given in Table 2, and the analysis conditions are given in Table 6. The physical calculation time interval was set to 0.001 s. For the non-dimensional EOM, when the number of elements was set to unity,

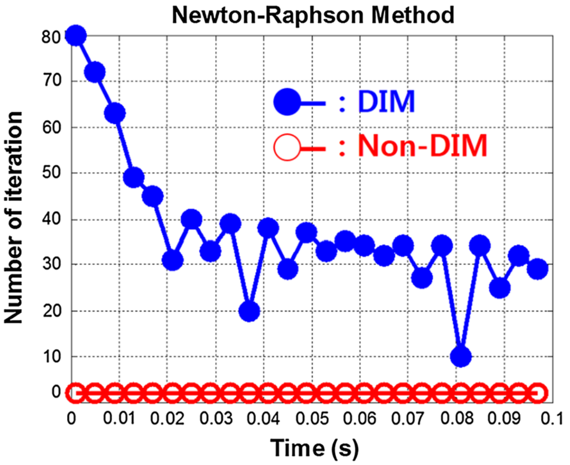

Fig. 7 Iteration number with Newton–Raphson method for each time step with dimensional and non-dimensional equations of motion

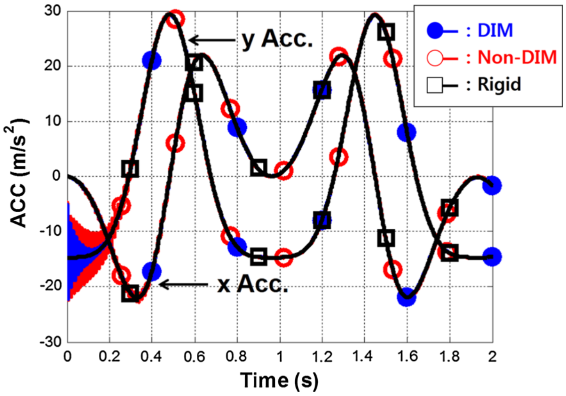

Fig. 9 End node acceleration of a simple pendulum using a rigid body model, and dimensional and non-dimensional equations of motion

the analysis time was shown to increase compared to the physical time. However, when the dimensional EOM was used, the calculation time increased instead. This happened because the Newton–Raphson method was used to find a solution to the next step during the process of finding a solution at each step. In the case of the non-dimensional EOM, the convergence to the solution increased compared to the convergence with the dimensional EOM. To explain this, Fig. 7 shows the iteration number for the convergence to a solution for dimensional and non-dimensional EOMs when finding the solution in the next step. With the dimensional EOM, the iteration number for the convergence to a solution increased considerably compared to the case of using a non-dimensional EOM. This means that the convergence to a solution decreased. In the case of the dimensional EOM, the initial step required approximately 80 iterations. In the case of the non-dimensional EOM, one or two iterations were required across the entire section. This phenomenon occurred because the convergence to a solution increased as the high-frequency components were canceled out through the non-dimensionalization of the EOM.

Figure 8 shows that the analysis results of a simple pendulum motion using a rigid body were consistent with the dimensional and non-dimensional EOMs. The figure also shows the acceleration information for

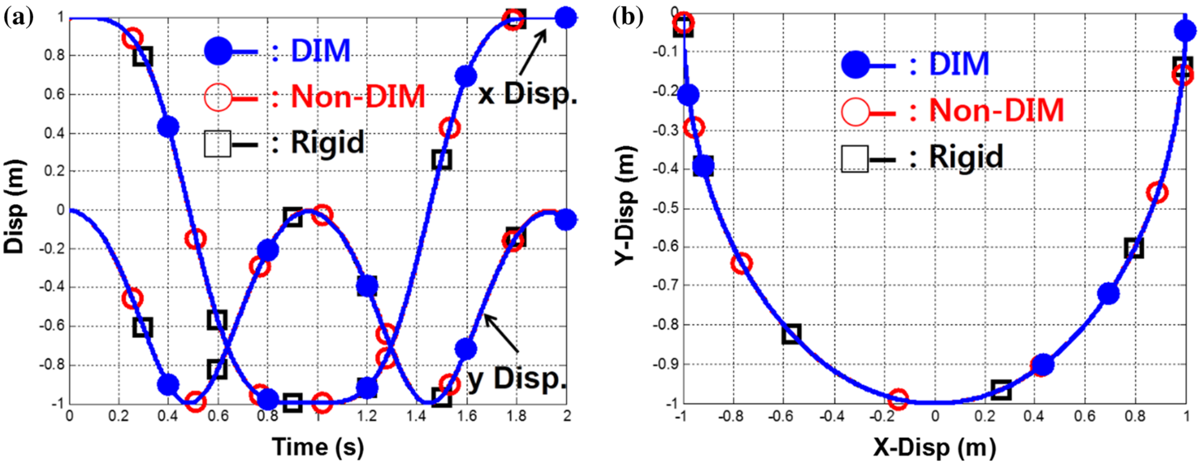

Fig. 8 End node position of a simple pendulum using a rigid body model, and dimensional and non-dimensional equations of motion. **a** Time versus *x* and *y* displacement, **b** *x* displacement versus *y* displacement

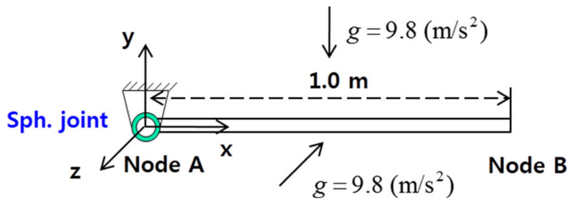

Fig. 10 Free-falling pendulum with spherical joint

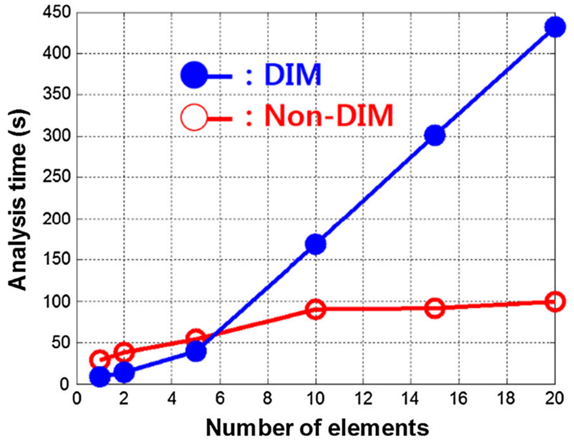

Fig. 11 Comparison of analysis times with dimensional and non-dimensional equations of motion

the x-axis and y-axis. For the dimensional and non-dimensional EOMs, the characteristics of the flexible body using absolute nodal coordinates were confirmed to be represented by the vibration phenomenon of the early behavior, and the vibration characteristics were offset by numerical damping (Fig. 9).

3.3 Free-falling pendulum with spherical joint

Based on the example of a free-falling pendulum with a spherical joint shown in Fig. 10, a case was considered in which one end is connected to a spherical joint, and a force with the magnitude of gravity is acting in the y-axis and z-axis directions simultaneously. The spherical joint facilitates three-axis rotation and is sensitive in numerical analysis, especially to numerical error. By using a spherical joint, the modeling accuracy when using absolute nodal coordinates and the robustness of the Newmark implicit integration method can be determined.

Figure 10 represents a situation in which the aforementioned spherical joint is connected and the force of gravity is simultaneously acting in the y-axis and z-axis directions. The specifications and properties for simple pendulum motion are given in Table 2. Because the spherical joint, which is sensitive to numerical analysis, was adopted, Young's modulus was reduced to 1/1000 of its value to maintain the analysis time interval. Table 3 gives the non-dimensional variable T_{ND} according to the number of elements. Table 7 shows the calculation times for a physical time of 2 s according to the simple pendulum motion when using dimensional and non-dimensional EOMs. Figure 11 shows a graph of the numerical values in Table 7. For the dimensional EOM, the calculation time linearly increases as the number of elements is increased. For the non-dimensional EOM, the calculation time was confirmed to converge to a single value as the non-dimensional variable T_{ND} increased.

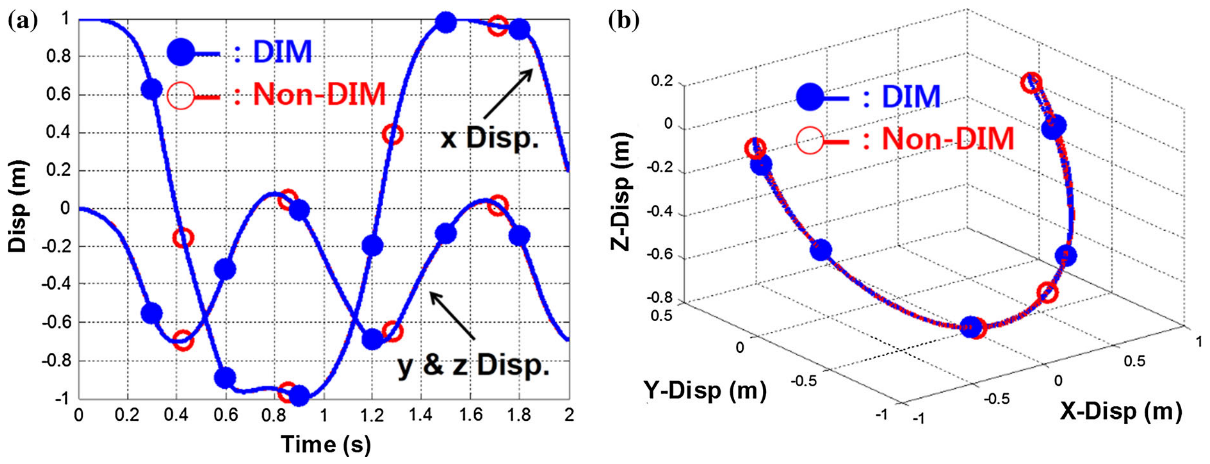

Fig. 12 End node position of simple pendulum attached to spherical joint with dimensional and non-dimensional equations of motion. **a** Time versus x and y displacement, **b** 3-D view

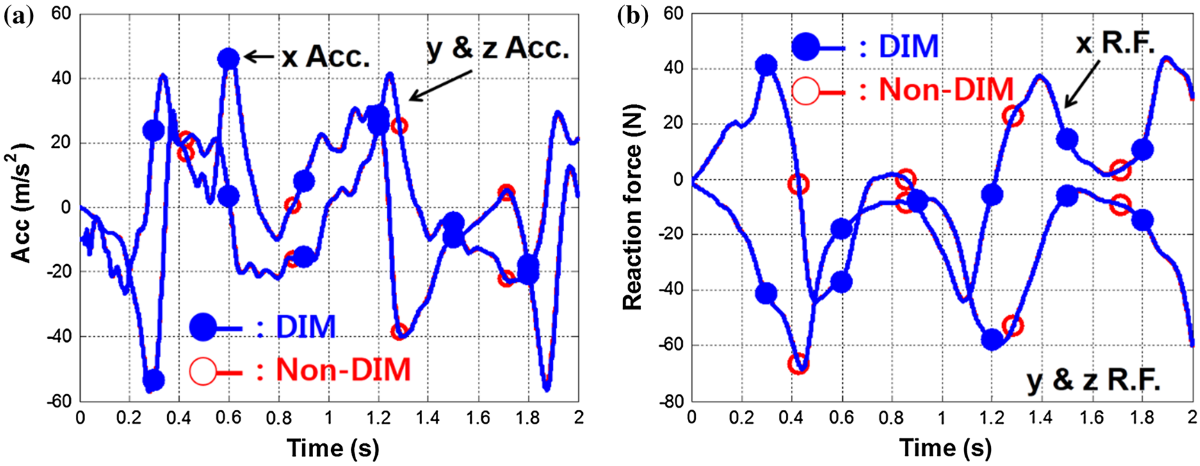

Fig. 13 Acceleration and reaction force of simple pendulum at the position of spherical joint with dimensional and non-dimensional equations of motion. **a** Time versus acceleration, **b** time versus reaction force

Figure 12 shows that the analysis results for a simple pendulum motion using dimensional and non-dimensional EOMs are in good agreement. In particular, despite the use of a sensitive spherical joint, the agreement of the y-axis and z-axis behavior results means that the modeling using absolute nodal coordinates is accurate. The agreement of the y-axis and z-axis behavior results can be considered to be an advantage that appears when using slopes in the absolute nodal coordinate formulation. Figure 13 shows the acceleration and reaction force information at the joint, the y-axis and z-axis were confirmed to have the same results. The variations in Fig. 13 occurred because Young's modulus was reduced to 1/1000 of its original value.

4 Conclusions

Studies of absolute nodal coordinate formulation began through related research on the finite element analysis of beams and beam formulations in 1996. One of the weaknesses of the absolute nodal coordinate system is that the analysis time increases with the number of DOF at the nodal point. To address this, the analysis time was reduced in this study by converting a dimensional equation of motion (EOM) to a non-dimensional EOM. To convert a dimensional EOM to non-dimensional EOM, the non-dimensional variables T_{ND}, L_{ND}, and F_{ND} (related to time, length, and force, respectively) were used. The 3-D non-dimensional model developed in this study is based on the 3-D model developed by Garcia-Vallejo et al. [22]. This was used to determine a non-dimensional mass matrix, non-dimensional stiffness matrix, and non-dimensional conservative force vector, as discussed in Sect. 2.

The non-dimensional EOM was verified by using examples of a cantilever beam and free-falling pendulum with revolute and spherical joints. First, the effectiveness of the non-dimensional EOM was verified by using a cantilever beam example for which an exact solution exists for static deflection. Increasing the number of elements of the cantilever beam was shown to prevent shear locking, which can occur in finite element analysis. The analysis time efficiency increased with the non-dimensional variable T_{ND}. Next, the example of a free-falling pendulum with a revolute joint confirmed that the Newton–Raphson method converged to a solution in the next step. With the non-dimensional EOM, the convergence speed noticeably increased compared to the case of using a dimensional EOM. The non-dimensional EOM was verified through a comparison with a simple pendulum motion modeled using a rigid body. The characteristics of the absolute nodal coordinate formulation were confirmed, wherein both the rigid body and elastic body characteristics can be expressed with the same formulation. Finally, the example of a free-falling pendulum with a spherical joint was considered. The usefulness of the non-dimensional EOM was verified by the adoption of a numerically sensitive spherical joint. In particular, when the pendulum was divided into 20 elements, the analysis time using a non-dimensional EOM was reduced more than fourfold. The end node position of the pendulum, the acceleration, and the reaction force occurring at the joint were confirmed to be consistent with the dimensional and non-dimensional EOMs.

The unique contributions of this study are as follows:

(1) The adoption of non-dimensional nodal coordinates for an absolute nodal coordinate formulation;
(2) The development of a 3D non-dimensional model with an absolute nodal coordinate formulation by the use of the non-dimensional variables T_{ND}, L_{ND}, and F_{ND} for the time, length, and force, respectively; and
(3) The verification of the non-dimensional EOM's numerical solution and analysis efficiency by using the examples of a cantilever beam and free-falling pendulum with revolute and spherical joints.

Acknowledgements This research was supported by the Korea Institute of Industrial Technology (KITECH) and the Agency for Defense Development (ADD).

Appendix

Discretizing Eq. (16) in Sect. 2.1 gives as follows:

$$\vec{\boldsymbol{\Psi}}\left(\frac{\mathrm{d}^2\hat{\vec{\mathbf{e}}}^*_{n+1}}{\mathrm{d}t^{*2}_{n+1}},\vec{\boldsymbol{\lambda}}_{n+1}\right) = \left\{\begin{array}{l} \mathbf{M}^*\left(\frac{\mathrm{d}^2\hat{\vec{\mathbf{e}}}^*_{n+1}}{\mathrm{d}t^{*2}_{n+1}}\right)+\boldsymbol{\Phi}^T_{\hat{\vec{\mathbf{e}}}^*_{n+1}}\vec{\boldsymbol{\lambda}}_{n+1}+\mathbf{K}^*(\hat{\vec{\mathbf{e}}}^*_{n+1})\hat{\vec{\mathbf{e}}}^*_{n+1}-\vec{\mathbf{F}}^*_C \\ \vec{\boldsymbol{\Phi}}\left(\hat{\vec{\mathbf{e}}}^*_{n+1}\right) \end{array}\right\} = \vec{\mathbf{0}} \tag{35}$$

Next, the Newmark formula for the numerical integration of the displacement and velocity is given by

$$\begin{cases} \hat{\vec{\mathbf{e}}}^*_{n+1}=\hat{\vec{\mathbf{e}}}^*_n+h\left(\frac{\mathrm{d}\hat{\vec{\mathbf{e}}}^*_{n+1}}{\mathrm{d}t^*_{n+1}}\right)+\frac{h^2}{2}\left[(1-2\beta)\left(\frac{\mathrm{d}^2\hat{\vec{\mathbf{e}}}^*_n}{\mathrm{d}t^{*2}_n}\right)+2\beta\left(\frac{\mathrm{d}^2\hat{\vec{\mathbf{e}}}^*_{n+1}}{\mathrm{d}t^{*2}_{n+1}}\right)\right] \\ \frac{\mathrm{d}\hat{\vec{\mathbf{e}}}^*_{n+1}}{\mathrm{d}t^*_{n+1}}=\frac{\mathrm{d}\hat{\vec{\mathbf{e}}}^*_n}{\mathrm{d}t^*_n}+h\left[(1-\gamma)\left(\frac{\mathrm{d}^2\hat{\vec{\mathbf{e}}}^*_n}{\mathrm{d}t^{*2}_n}\right)+\gamma\left(\frac{\mathrm{d}^2\hat{\vec{\mathbf{e}}}^*_{n+1}}{\mathrm{d}t^{*2}_{n+1}}\right)\right] \end{cases} \tag{36}$$

where n is the current step, $n+1$ is the next step for which a solution is to be found, and h is the time integration interval. In Eq. (36), the coefficients β and γ are arbitrary constants, and common values for them are given in Table 7. When finding the solution of the next step, the Newton–Raphson method is usually used to improve the convergence rate. This requires the use of a Jacobian matrix. Because Eq. (35) is expressed as a function of $d^2\hat{\vec{\mathbf{e}}}^*_{n+1}/dt^{*2}_{n+1}$ and λ_{n+1} by its relationship with Eq. (36), the chain rule can be used to express the Jacobian matrix as follows:

Table 7 Some of the most commonly used modified Newmark methods

	γ	β	Accuracy
Central difference	1/2	0	Excellent for small h Unstable for large h
Linear acceleration	1/2	1/6	Very good for small h Unstable for large h
Average acceleration	1/2	1/4	Good for small h No energy dissipation
ADAMS [38]	0.70	0.36	–

$$\mathbf{J}=\begin{bmatrix}\frac{\partial\vec{\boldsymbol{\Psi}}}{\partial\left(\frac{\mathrm{d}^2\hat{\vec{\mathbf{e}}}^*}{\mathrm{d}t^{*2}}\right)} & \frac{\partial\vec{\boldsymbol{\Psi}}}{\partial\vec{\boldsymbol{\lambda}}}\end{bmatrix} = \begin{bmatrix}\mathbf{M}^*+\beta h^2\left(\frac{\partial\left(\boldsymbol{\Phi}^T_{\hat{\vec{\mathbf{e}}}^*}\vec{\boldsymbol{\lambda}}\right)}{\partial\hat{\vec{\mathbf{e}}}^*}+\frac{\partial\left(\mathbf{K}^*(\hat{\vec{\mathbf{e}}}^*)\hat{\vec{\mathbf{e}}}^*\right)}{\partial\hat{\vec{\mathbf{e}}}^*}\right) & \boldsymbol{\Phi}^T_{\hat{\vec{\mathbf{e}}}^*} \\ \beta h^2\boldsymbol{\Phi}_{\hat{\vec{\mathbf{e}}}^*} & \mathbf{0}\end{bmatrix} \tag{37}$$

When Eq. (37) is used, the increment for the solution in the next stage can be obtained with Eq. (38):

$$\left\{\begin{array}{l}\delta\left(\frac{\mathrm{d}^2\hat{\vec{\mathbf{e}}}^*}{\mathrm{d}t^{*2}}\right) \\ \delta\vec{\boldsymbol{\lambda}}\end{array}\right\} = \begin{bmatrix}\mathbf{M}^*+\beta h^2\left(\frac{\partial\left(\boldsymbol{\Phi}^T_{\hat{\vec{\mathbf{e}}}^*}\vec{\boldsymbol{\lambda}}\right)}{\partial\hat{\vec{\mathbf{e}}}^*}+\frac{\partial\left(\mathbf{K}^*(\hat{\vec{\mathbf{e}}}^*)\hat{\vec{\mathbf{e}}}^*\right)}{\partial\hat{\vec{\mathbf{e}}}^*}\right) & \boldsymbol{\Phi}^T_{\hat{\vec{\mathbf{e}}}^*} \\ \beta h^2\boldsymbol{\Phi}_{\hat{\vec{\mathbf{e}}}^*} & \mathbf{0}\end{bmatrix}^{-1} \cdot\vec{\boldsymbol{\Psi}}\left(\frac{\mathrm{d}^2\hat{\vec{\mathbf{e}}}^{*(i)}}{\mathrm{d}t^{*2}},\vec{\boldsymbol{\lambda}}^{(i)}\right) \tag{38}$$

Therefore, the solution in the next stage can be determined with Eq. (39) based on the convergence tolerance of the solution and the current step's solution and increment.

$$\left\{\begin{array}{l}\left(\frac{\mathrm{d}^2\hat{\vec{\mathbf{e}}}^*}{\mathrm{d}t^{*2}}\right) \\ \vec{\boldsymbol{\lambda}}\end{array}\right\}^{(i+1)} = \left\{\begin{array}{l}\left(\frac{\mathrm{d}^2\hat{\vec{\mathbf{e}}}^*}{\mathrm{d}t^{*2}}\right) \\ \vec{\boldsymbol{\lambda}}\end{array}\right\}^{(i)} - \left\{\begin{array}{l}\delta\left(\frac{\mathrm{d}^2\hat{\vec{\mathbf{e}}}^*}{\mathrm{d}t^{*2}}\right) \\ \delta\vec{\boldsymbol{\lambda}}\end{array}\right\} \tag{39}$$

References

1. Shabana, A.A.: An Absolute Nodal Coordination for the Large Rotation and Large Deformation analysis of Flexible Bodies. Technical Report, No.MBS96-1-UIC (1996)

2. Shabana, A.A.: Definition of the slopes and the finite element absolute nodal coordinate formulation. Multibody Syst. Dyn. **1**, 339–348 (1997)
3. Shabana, A.A., Hussein, H.A., Escalona, J.L.: Application of the absolute nodal coordinate formulation to large rotation and large deformation problems. J. Mech. Des. **120**(2), 188–195 (1998)
4. Escalona, J.L., Hussien, H.A., Shabana, A.A.: Application of the absolute nodal co-ordinate formulation to multibody system dynamics. J. Sound Vib. **214**(5), 833–851 (1998)
5. Omar, M.A., Shabana, A.A.: Two-dimensional shear deformable beam for large rotations and deformation problems. J. Sound Vib. **243**, 565–576 (2001)
6. Shabana, A.A., Yakoub, R.Y.: Three dimensional absolute nodal coordinate formulation for beam elements: theory. ASME J. Mech. Des. **123**, 606–613 (2001)
7. Yakoub, R.Y., Shabana, A.A.: Three dimensional absolute nodal coordinate formulation for beam elements: implementation and application. ASME J. Mech. Des. **123**, 614–621 (2001)
8. Shabana, A.A.: Dynamics of Multibody Systems, 3rd edn. Cambridge University Press, New York (2005)
9. Berzeri, M., Shabana, A.A.: Development of simple models for the elastic forces in the absolute nodal co-ordinate formulation. J. Sound Vib. **235**(4), 539–565 (2000)
10. Shabana, A.A.: Computational Continuum Mechanics. Cambridge University Press, New York (2008)
11. Gerstmayr, J., Sugiyama, H., Mikkola, A.: An overview on the developments of the absolute nodal coordinate formulation. In: The 2nd Joint International Conference on Multibody System Dynamics (2012)
12. Dmitrochenko, O., Yoo, W.S., Pogorelov, D.: Helicoseir as shape of a rotating string (I): 2D theory and simulation using ANCF. Multibody Syst. Dyn. **15**, 135–158 (2006)
13. Dmitrochenko, O., Yoo, W.S., Pogorelov, D.: Helicoseir as shape of a rotating string (II): 3D theory and simulation using ANCF. Multibody Syst. Dyn. **15**, 181–200 (2006)
14. Yoo, W.S., Lee, J.H., Park, S.J., Sohn, J.H., Dmitrochenko, O., Pogorelov, D.: Large oscillations of a thin cantilever beam: physical experiments and simulation using the absolute nodal coordinate formulation. Nonlinear Dyn. **34**, 3–29 (2003)
15. Yoo, W.S., Dmitrochenko, O., Park, S.J., Lim, O.K.: A new thin spatial beam element using the absolute nodal coordinates: application to rotating strip. Mech. Des. Struct. Mech. **33**, 399–422 (2005)
16. Yoo, W.S., Park, S.J., Dmitrochenko, O., Pogorelov, D.Y.: Verification of absolute nodal coordinate formulation in flexible multibody dynamics via physical experiments of large deformation problems. J. Comput. Nonlinear Dyn. **1**(1), 81–93 (2006)
17. Kim, K.W., Lee, J.W., Yoo, W.S.: The motion and deformation rate of a flexible hose connected to a mother ship. J. Mech. Sci. Technol. **26**(3), 703–710 (2012)
18. Sugiyama, H., Suda, Y.: Nonlinear elastic ring tire model using the absolute nodal coordinate formulation. IMechE J. Multi-Body Dyn. **223**, 211–219 (2009)
19. Rao, S.S.: Mechanical Vibrations, Fifth edn. Pearson Education Asia, Singapore (2011)
20. Sugiyama, H., Koyama, H., Yamashita, H.: Gradient deficient curved beam element using the absolute nodal coordinate formulation. J. Comput. Nonlinear Dyn. **5**(2), 1–8 (2010)
21. Timoshenko, S.P.: History of Strength of Materials. Dover Publications, New York (1983)
22. Garcia-Vallejo, D., Mayo, J., Escalona, L., Dominguez, J.: Efficient evaluation of the elastic forces and the Jacobian in the absolute nodal coordinate formulation. Nonlinear Dyn. **35**, 313–329 (2004)
23. Sopanen, J.T., Mikkola, A.K.: Description of elastic forces in absolute nodal coordinate formulation. Nonlinear Dyn. **34**, 53–74 (2003)
24. Gerstmayr, J., Shabana, A.A.: Analysis of thin beams and cables using the absolute nodal co-ordinate formulation. Nonlinear Dyn. **45**, 109–130 (2006)
25. Matikanen, M.K., Dmitrichenko, O.N., Mikkola, A.M.: Beam elements with trapezoidal cross section deformation modes based on the absolute nodal coordinate formulation. In: International Conference on Numerical Analysis and Applied Mathematics, pp. 1266–1270 (2010)
26. Kawaguti, K., Terumich, Y., Takehara, S., Kaczmarczylk, S., Sogabe, K.: The study of the tether motion with time-varying length using the absolute nodal coordinate formulation with multiple nonlinear time scales. J. Syst. Des. Dyn. **1**(3), 491–500 (2007)
27. Nikravesh, P.E.: Computer-Aided Analysis of Mechanical Systems. Prentice-Hall International Inc, Englewood Cliffs (1988)
28. Brenam, K.E., Campbell, S.L., Petzold, L.R.: Numerical Solution of Initial-Value Problems in Differential-Algebraic Equations. SIAM, Philadelphia, PA (1996)
29. Newmark, N.M.: A method of computation for structural dynamics. ASCE J. Eng. Mech. Div. **85**, 67–94 (1959)
30. Bathe, K.J.: Finite Element Procedures. Prentice Hall International Inc., Englewood Cliffs (1996)
31. Crisfield, M.A.: Nonlinear Finite Element Analysis of Solids and Structures. Wiley, New York (1997)
32. http://www.mathworks.com/
33. Valipour, M.: Optimization of neural networks for precipitation analysis in a humid region to detect drought and wet year alarms. Meteorol. Appl. **23**(1), 91–100 (2016)
34. Valipour, M., Banihabib, M.E., Behbahani, S.M.R.: Comparison of the ARMA, ARIMA, and the autoregressive artificial neural network models in forecasting the monthly inflow of Dez dam reservoir. J. Hydrol. **476**(7), 433–441 (2013)
35. Valipour, M., Sefidkouhi, M.A.G., Eslamian, S.: Surface irrigation simulation models: a review. Int. J. Hydrol. Sci. Technol. **5**(1), 51–70 (2015)
36. Valipour, M.: Sprinkle and trickle irrigation system design using tapered pipes for pressure loss adjusting. J. Agric. Sci. **4**(12), 125–133 (2012)
37. Khasraghi, M.M., Sefidkouhi, M.A.G., Valipour, M.: Simulation of open- and closed-end border irrigation systems using SIRMOD. Arch. Agron. Soil Sci. **61**(7), 929–941 (2015)
38. http://www.mscsoftware.com/